Chemical Science

ROYAL SOCIETY OF CHEMISTRY

EDGE ARTICLE

View Article Online
View Journal | View Issue

Cite this: *Chem. Sci.*, 2025, **16**, 4821

All publication charges for this article have been paid for by the Royal Society of Chemistry

A novel Ln^{3+}/Al^{3+} metallacrown multifunctional material for latent fingerprint detection, luminescent thermometers and luminescent sensors†

Han Yan,[a] Claudia M. S. Calado,[b] Hao Wang,[a] Muralee Murugesu *[b] and Wen-Bin Sun *[a]

Lanthanide luminescent complexes are active and thriving in various research fields due to their unique optical properties, while optical materials across a wide spectral range and with multiple functions in one were rarely reported. In this work, a new class of Ln^{3+}/Al^{3+} metallacrowns (MCs) were constructed with excellent luminescence properties in both the visible and near-infrared regions, and the elaborate luminescence modulation can be achieved by doping with different Ln^{3+} ions. Strikingly, the powder of **LnMC** was developed as a luminescent nanomaterial for the detection of latent fingerprints (LFPs), and even the third level details of fingerprints can be clearly recognized, which provides a reference for the identification of fingerprints in the field of criminal investigation. More importantly, **TbMC** and $Tb_{0.1}Sm_{0.9}$**MC** can be successfully used as luminescent thermometers with sensitivities of 2.51% $°C^{-1}$ and 2.33% $°C^{-1}$, respectively, higher than most reported values. Meanwhile, **TbMC** was developed as a luminescent probe for Fe^{3+} and 2,6-pyridinedicarboxylic acid (DPA) with low limits of detection (LOD) of 0.51 μM and 4.26 μM, respectively, representing the first example of MC with luminescence sensing. Also of note is that **SmMC**, $Tb_{0.1}Sm_{0.9}$**MC** and **TbMC** can be functionalized as luminescent inks and films due to their clear recognizable colours in the visible range, suggesting a new strategy for high-level anti-counterfeiting. In short, the **LnMC** luminescent material has wide application prospects in many fields, especially rare for multifunctional applications of small-molecule complexes with non-metal–organic frameworks.

Received 18th December 2024
Accepted 29th January 2025

DOI: 10.1039/d4sc08549c

rsc.li/chemical-science

Introduction

Metallacrowns (MCs) are a class of multinuclear metal macrocyclic organic complexes that can be viewed as inorganic analogues of standard crown ether rings in which the alkyl carbon atoms are replaced by transition metal ions and nitrogen atoms to form metal–heteroatom repeating-[M–N–O]–$_n$ coordination units.[1–3] The coordination cavities of the MC macrocycles provide oxygen coordination sites for encapsulation of different metal cation centers.[4,5] Attributed to their unique topology, MCs have been widely used in many research areas, such as molecular recognition,[6,7] catalysis,[8,9] bioactivity,[10,11] and single-molecule magnets,[12,13] but have been slow to progress in luminescence. Lanthanides are ideal candidates for the preparation of luminescent materials because of their inherent large Stokes shifts, narrow emission spectra, and long lifetimes, which enable high colour purity emission in the visible and near-infrared ranges.[14–18] However, the Laporte forbidden 4f–4f electron transition of Ln^{3+} results in very weak luminescence under direct excitation.[19] Fortunately, this low molar absorption coefficient can be overcome by the "antenna effect" with the help of ligands.[20] It was not until 2011 that Pecoraro reported the first Ln^{3+} MC with Zn^{2+} ion ring metals, realizing NIR luminescence of Nd^{3+} and Yb^{3+}, opening the door to the luminescence field of MCs.[21] Subsequently, a series of Ga^{3+}/Ln^{3+} MC families with excellent luminescence properties have been continuously developed and breakthroughs have been achieved.[22–25] However, such complexes rarely have functionalized applications or are only monofunctional.[26,27] Therefore, there is a pressing imperative for developing multifunctional Ln-based MC complexes to meet the demands of a wide range of fields.

Human fingerprints vary in patterns, breaks and crossings, and relying on their uniqueness and lifelong invariance, fingerprint identification is an effective means of verifying an

[a]*Key Laboratory of Functional Inorganic Material Chemistry Ministry of Education, School of Chemistry and Material Science, Heilongjiang University, 74 Xuefu Road, Harbin 150080, P. R. China. E-mail: wenbinsun@126.com*

[b]*Department of Chemistry and Biomolecular Sciences, University of Ottawa, Ottawa, Ontario K1N 6N5, Canada. E-mail: m.murugesu@uottawa.ca*

† Electronic supplementary information (ESI) available: General experimental section, including all procedures and equipment used. CCDC 2377154. For ESI and crystallographic data in CIF or other electronic format see DOI: https://doi.org/10.1039/d4sc08549c

individual's identity.[28] Therefore, it is necessary to develop detection materials for latent fingerprints (LFPs) to provide valuable evidence for forensic science.[29,30] Simultaneously, temperature is closely related to human activities, and its precise measurement is essential in scientific research, daily life, and industry.[31–33] Currently, non-contact luminescent thermometers have become an emerging method for temperature measurement.[34,35] Luminescent thermometers operate by monitoring an optical signal, such as luminescence intensity or luminescence lifetime, in response to temperature changes, offering non-invasive, convenient, and sensitive detection.[36,37] Moreover, it is necessary to monitor heavy metals and pathogenic spores to ensure environmental health safety and biological health.[38,39] Among them, the first and foremost are Fe^{3+} and 2,6-pyridinedicarboxylic acid (DPA) (a biomarker for *Bacillus anthracis* spores), the former being highly toxic and non-biodegradable, seriously affecting biological health, and the latter posing a serious threat to life safety as an acute infectious disease with high lethality.[40–42] In addition, the advent of the information age has promoted rapid economy development, but serious problems of information leakage and counterfeiting have also followed.[43–45] This not only raises concerns about information security but also causes economic losses.[46] As a result, it is urgent to develop multifunctional materials integrating clear LFP detection, high sensitivity luminescent thermometers, highly selective luminescence sensing, and new anti-counterfeiting technologies.

The selection of ligands matching the energy levels of the lanthanide centers is a key factor in the preparation of luminescent sensing materials. Therefore, in this work, we chose the salicylhydroxamic acid (H_3shi) and sodium *p*-hydroxybenzoate ligands to act as antennas to transmit the excited energy to sensitize the lanthanide centers. A series of novel **LnMC** compounds exhibiting luminescence emission from the visible to near-infrared range were successfully prepared using trivalent aluminum ions, and luminescence modulation was achieved by energy transfer between Tb^{3+} and Sm^{3+} ions. The application of LFP detection is supported by the bright luminescence of **LnMC** in the visible region, allowing clear identification of the third level of fingerprint details. Meanwhile, the energy transfer between lanthanide ions is intriguing, and the luminescence modulation was favorably achieved by chemically adjusting the molar ratio of Tb^{3+}/Sm^{3+}. Furthermore, the potential of **TbMC** and **$Tb_{0.1}Sm_{0.9}$MC** as luminescent thermometers was systematically explored with sensitivities of 2.51% $°C^{-1}$ and 2.33% $°C^{-1}$, respectively, which are comparable to or better than other lanthanide-based luminescent thermometers reported in the literature. In addition, the bright green emission endows **TbMC** with a luminescent sensor for the detection of Fe^{3+} and DPA with a limit of detection (LOD) in the low-level range, and the corresponding test papers have been successfully prepared, which can be used for rapid detection in the field. Notably, **LnMC** has been functionally developed as anti-counterfeiting inks and films, enabling multi-level encryption of information and anti-counterfeiting labels. Overall, the Ln^{3+}/Al^{3+} MC has excellent luminescence properties with luminescence emission covering almost the full range of the spectral domain and can also be used for LFP detection, for luminescent thermometers and multi-responsive luminescent sensing materials, as well as for anti-counterfeiting applications, which are rare for small-molecule complexes with non-metal–organic frameworks.

Results and discussion

Synthesis and crystal structures

LnMC was synthesized by a one-pot method using H_3shi, lanthanide nitrate, aluminum nitrate, and excess of sodium *p*-hydroxybenzoate. Crystals of **DyMC** of suitable size and quality for X-ray diffraction were obtained, and the corresponding packing diagram is provided in Fig. S1.† Thermogravimetric analysis of **DyMC** is shown in Fig. S2.† PXRD analysis confirmed that all **LnMC** are isostructural (Fig. S3†), allowing a comprehensive discussion of their molecular structures. **DyMC** crystallizes in a tetragonal space group (Table S1†), and the crystal structure is shown in Fig. 1. Four deprotonated shi^{3-} ligands bridge four Al^{3+} ions to form four Al–N–O repeating units, resulting in a square-shaped neutral 12-MC-4 macrocycle. Four *p*-hydroxybenzoate ligands bridge the Dy^{3+} ion and the four Al^{3+} ions anchor the central Dy^{3+} ion above the MC ring constituting an eight-coordinate square antiprism geometry (Fig. 1d), which is confirmed by Continuous Shape Measure (CShM)[47] analysis (Table S3†). The carboxylic acid groups bridging the Dy^{3+} ion and the Al^{3+} ion on the ring provides additional stability to the MC scaffolds. The sodium ion is located on the opposite side of the MC, bridged by water molecules, providing charge balance.

Photophysical properties

The complex electronic structure of the trivalent lanthanide ions endows Ln^{3+} with unique optical properties and exhibits characteristic luminescence.[48] Photoluminescence spectra are

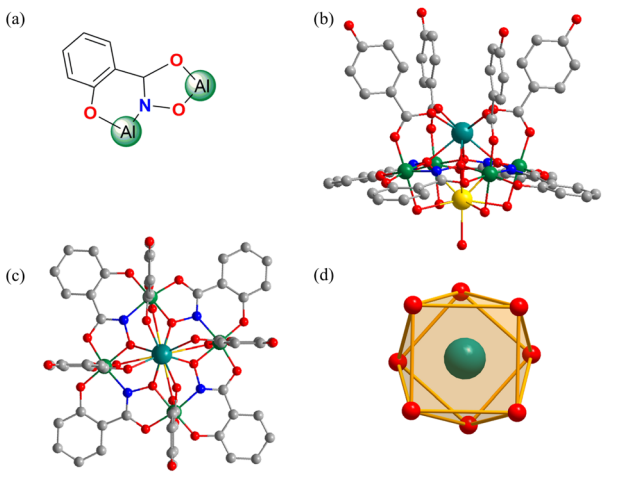

Fig. 1 (a) Coordination mode of the shi^{3-} ligand. Partially labeled molecular structure of **DyMC**: (b) side view and (c) top-down view. H atoms and the solvent are omitted for clarity. Colour code: Dy (teal), Al (green), O (red), N (blue), C (grey), and Na (yellow). (d) Coordination geometry around the central Dy^{3+} ion.

an important means of investigating the spectral properties of materials. The excitation spectra of **LnMC** (Ln = Sm, Eu, Tb, Dy, Ho, Er, Yb) were collected within the 200–400 nm range, and all of the absorption peaks showed an intense band at 336 nm, which is attributed to the same ligand (Fig. 2a). Therefore, the luminescence emission spectra of **LnMC** were recorded from visible to near-infrared domains under 336 nm excitation. For **SmMC**, characteristic emission peaks of Sm^{3+} were detected; four peaks were observed at 560, 597, 640 and 698 nm in the visible region corresponding to $^4G_{5/2} \rightarrow {}^6H_J$ (J = 5/2–11/2) transitions, and three peaks were also observed at 892, 935 and 1016 nm in the near-infrared range assigning to $^4G_{5/2} \rightarrow {}^6F_J$ (J = 5/2–11/2) transitions. **EuMC** showed typical emission peaks at 590, 615, 650, and 697 nm, arising from $^5D_0 \rightarrow {}^7F_J$ (J = 1–4) energy level transitions, where the most intense emission peak appears at 697 nm ($^5D_0 \rightarrow {}^7F_4$), leading to the emission of strong red light. Similarly, **TbMC** exhibited Tb^{3+} absorption bands with peaks at 490, 545, 581, and 618 nm due to transitions from the ground state $^5D_4$ to different excited levels ^7F_J (J = 6–3). **DyMC** displayed prominent characteristic emission in both the visible and near-infrared ranges with peaks at 480, 571, 660, 746, 834 and 1009 nm, which are assignable to the $^4F_{9/2} \rightarrow {}^6H_{15/2}$, $^4F_{9/2} \rightarrow {}^6H_{13/2}$, $^4F_{9/2} \rightarrow {}^6H_{11/2}$, $^4F_{9/2} \rightarrow {}^6H_{9/2}$, $^4F_{9/2} \rightarrow {}^6H_{7/2}$+$^6F_{9/2}$ and $^4F_{9/2} \rightarrow {}^6F_{7/2}$ energy level transitions, respectively. It is worth mentioning that the visible range is mainly dominated by $^4F_{9/2} \rightarrow {}^6H_{15/2}$ and $^4F_{9/2} \rightarrow {}^6H_{13/2}$ bands, resulting in near-standard white light emission from **DyMC** with CIE colour coordinates of (0.311, 0.359) and a correlated colour temperature equal to 6398 K. For the remaining **HoMC**, **ErMC** and **YbMC**, all generated near-infrared emission bands. In detail, **HoMC** obtained two peaks at 975 and 1172 nm corresponding to $^5F_5 \rightarrow {}^5I_7$ and $^5I_6 \rightarrow {}^5I_8$ energy level transitions. **ErMC** and **YbMC** exhibited fascinating long-wavelength emissions centered at 1538 nm ($^4I_{13/2} \rightarrow {}^4I_{15/2}$) and 975 nm ($^2F_{5/2} \rightarrow {}^2F_{7/2}$), respectively, with the full width at half maxima (FWHM) of about 1.47 × 10^5 cm^{-1} and 1.7 × 10^5 cm^{-1}, which offer the possibility of developing Er^{3+}/Yb^{3+}-doped fiber lasers. These results indicate that the ligand is able to effectively sensitize most of the Ln^{3+} ions, allowing **LnMC** to exhibit excellent lanthanide emission properties from the visible to the near-infrared region (Fig. 2a).

To further explore energy transfer, it is necessary to determine the triplet state (T_1) energy levels of the ligand. The Gd^{3+} ion complex is an effective probe for assessing the T_1, which has a sufficiently high first excited energy level (32 000 cm^{-1}) to avoid energy transfer from the ligand to the Gd^{3+} ion.[49] **GdMC** was investigated in the solid state using steady-state and time-resolved luminescence at −196 °C (77 K). Steady-state excitation and emission spectra (Fig. 2b) exhibit the expected ligand bands. To determine the exact position of the excited triplet state in this system, time-resolved emission measurements were conducted with a delay to eliminate singlet (S_1) emission. Initially, we hypothesized that the first band (centered at 460 nm) in the emission spectrum was assigned to S_1, while the second band (centered at 520 nm) was attributed to T_1. However, regardless of the applied delay, either the first emission band was always present, or the entire signal, including the second band, was eliminated. No significant changes were observed in the band after the delay, except for the noise-to-signal ratio (Fig. S4†). This suggests that both bands are likely assigned to two T_1 states from the two ligands present in the system, deprotonated shi^{3-} and *p*-hydroxybenzoate, rather than S_1 and T_1 emissions. Since the two components of the states could not be separated, it was not possible to calculate the lowest T_1 from which the electronic population would transfer to the Ln^{3+}. However, this value should not differ significantly from the one previously reported in the literature for a similar MC system, approximately at 22 200 cm^{-1}.[50] This energy level is located at an ingenious position which allows the ligand to transfer energy to most of the Ln^{3+} ions through the antenna effect. Meanwhile, the UV-visible absorption spectra of the ligand H_3shi, sodium *p*-hydroxybenzoate and **GdMC** in ethanol solution were analyzed. As shown in Fig. 2c, the absorption bands observed with the maxima at 294 nm in the spectrum of sodium *p*-hydroxybenzoate and at 283 nm and 358 nm in the spectrum of H_3shi could be attributed to π → π* transitions. The formation of a **GdMC** framework caused a redshift of the absorption band and exhibited a broad absorption band that extends from 200 to 400 nm (Fig. 2c).

A series of bimetallic centered **$Tb_{1-x}Sm_x$MC** (x = 0, 0.1, 0.3, 0.5, 0.7, 0.9, 1.0) co-doped with varying Tb^{3+}/Sm^{3+} molar ratios were synthesized for further explorations. It is noteworthy that the varying molar ratios of Tb^{3+} and Sm^{3+} lead to different luminescence colours of **$Tb_{1-x}Sm_x$MC**; as the Sm^{3+} ion content increases, the characteristic emission intensity of Tb^{3+} ions significantly decreases, and the luminescence colour of **$Tb_{1-x}Sm_x$MC** under 336 nm excitation turns from green to yellow-green, yellow, and orange-red (Fig. 3a). This implies the existence of an energy transfer from Tb^{3+} to Sm^{3+}, which successfully realizes a series of multicolour emissions of **$Tb_{1-x}Sm_x$MC**. In addition, the CIE chromaticity diagram in clearly shows the process of colour change; the CIE colour coordinates of

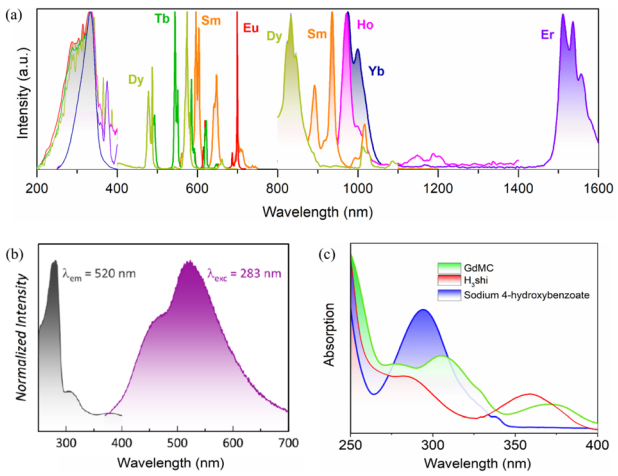

Fig. 2 (a) Normalized excitation and emission spectra of **LnMC** systems in the solid state, under ligand excitation (336 nm) at room temperature. (b) Steady-state excitation (gray) and emission (violet) spectra of **GdMC** obtained at 77 K. (c) UV-vis absorption spectra of the ligands and **GdMC** in ethanol.

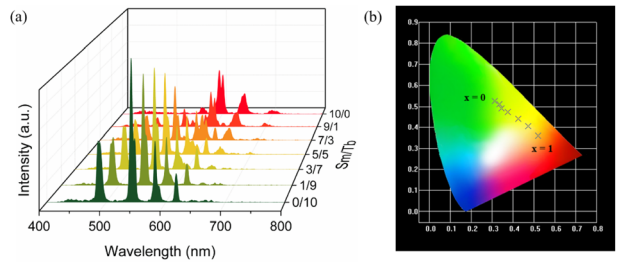

Fig. 3 (a) Emission spectra and (b) the corresponding CIE chromaticity diagram of $Tb_{1-x}Sm_xMC$.

$Tb_{1-x}Sm_xMC$ ($x = 0$, 0.1, 0.3, 0.5, 0.7, 0.9, 1.0) are (0.313, 0.525), (0.334, 0.511), (0.346, 0.490), (0.375, 0.473), (0.426, 0.440), (0.472, 0.405), and (0.521, 0.361), respectively (Fig. 3b).

Latent fingerprint detection

The uniqueness of human fingerprints makes fingerprint recognition an important measure of identification, which is widely used in forensic science, security authentication and other fields.[51–53] Powder dusting as an LFP visualization technology, with high sensitivity and simple operation, plays an important role in criminal investigation.[54,55] **LnMC** as a luminescent nanomaterial has the potential to be developed into LFP detection materials attributed to its small size, low cost, and significant luminescence. All fingerprints were collected from the same volunteer. The volunteer pressed one finger on the glass to leave a fingerprint, following which **TbMC** powder was carefully sprinkled on the fingerprint, and the excess powder was then gently blew away with a rubber suction bulb to obtain a **TbMC**-stained LFP (Fig. 4a). Under UV light, the luminescence image of the LFP is clearly visible, as shown in Fig. 4b, and the first level macroscopic features including the (1) core and the second level details such as the (2) scar, (3) island, (4) bifurcation and (5) ridge termination of the fingerprint were recognized obviously. In particular, the third level details of (6) sweat pores were also clearly recognized by the naked eye (Fig. 4b), which provide a reference for authenticating the identity in criminal science. Notably, we also developed LFP detection for **SmMC** (Fig. 4c) and $\mathbf{Tb_{0.1}Sm_{0.9}MC}$ (Fig. 4d), and the generated fingerprint images are rendered in red and yellow respectively. The multicoloured LFP meets the needs of various environments and effectively avoids the interference of different backgrounds in the crime scene, which provides a promising method for identifying LFPs in criminal cases.

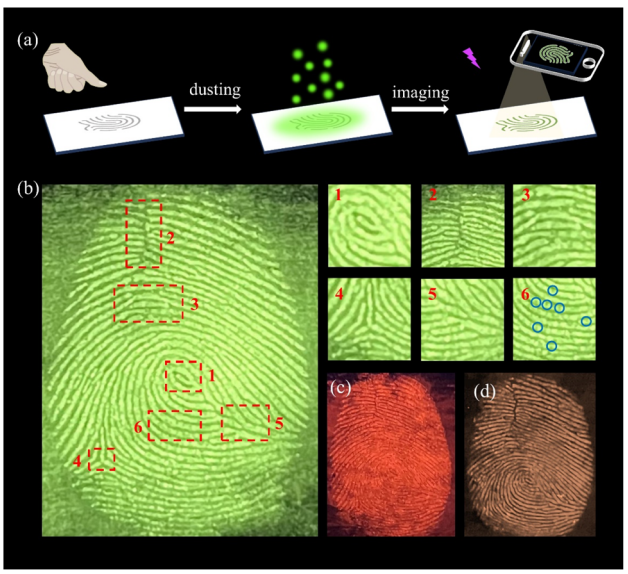

Fig. 4 (a) Schematic of LFP detection. (b) High resolution image of an LFP on glass visualized by **TbMC** powder under UV light and magnified images of fingerprint details like (1) core, (2) scar, (3) island, (4) bifurcation, (5) ridge termination and (6) sweat pores. Images of the LFP detected using (c) **SmMC** and (d) $Tb_{0.1}Sm_{0.9}MC$ under UV light.

Luminescent thermometers

The fascinating photophysical properties of **LnMC** in the visible region have aroused interest in exploring its potential as a luminescent thermometer. **LnMC** is stable in ethanol solution, and its luminescence intensity hardly changes after 24 h, which makes it a suitable solvent for testing (Fig. S5†). Initial luminescence measurements in ethanol solution (1 mg mL^{-1}) were conducted on homometallic samples. Upon excitation at 336 nm, the characteristic sharp emission bands of Tb^{3+} ($^5D_4 \rightarrow {}^7F_J$) in the visible range were observed (Fig. S6†). Similar results were obtained for the **SmMC** system regarding the excitation profile (Fig. S6†), as well as typical Sm^{3+} ($^4G_{5/2} \rightarrow {}^6H_J$) emission bands. The absence of noticeable intraconfigurational 4f–4f transitions in the excitation spectrum indicates a highly efficient antenna effect. The excited state emission decay curves of **LnMC** were measured by monitoring the most intense emission band of Tb^{3+} (545 nm) and Sm^{3+} (597 nm) upon excitation at 336 nm. In both cases, a monoexponential decay curve was observed, yielding a lifetime (τ) of 1011 μs for **TbMC** and 69 μs for **SmMC** (Fig. S7†).

To gain a better understanding of the system and its emission kinetics, emission decay curves for both systems were measured across a temperature range of 5–60 °C. It is observed that as the temperature increases, τ_{Tb} decreases (Fig. 5a), while τ_{Sm} remains nearly constant throughout the studied temperature range (Fig. 5b). This suggests that a back energy transfer (BET) from Tb^{3+} ($^5D_4$ at 20 500 cm^{-1}) to the ligand T_1 might occur as the temperature increases, due to the closer proximity of these states. In contrast, the larger energy gap between Sm^{3+} ($^4G_{5/2}$ at 17 900 cm^{-1}) and T_1 prevents that from happening. The lifetimes for both systems are summarized in Table S4,† with the small variation in τ_{Sm} being within the instrument's error.

$$y = \frac{A_1 + A_2}{1 + e^{(x-x_0)/dx}} + A_2 \quad (1)$$

Given its temperature dependence behaviour, τ_{Tb} was explored as the thermometric parameter (Δ). A Boltzmann-like function (eqn (1)), though without physical significance, was used to fit the thermometric parameter (Fig. 5c).

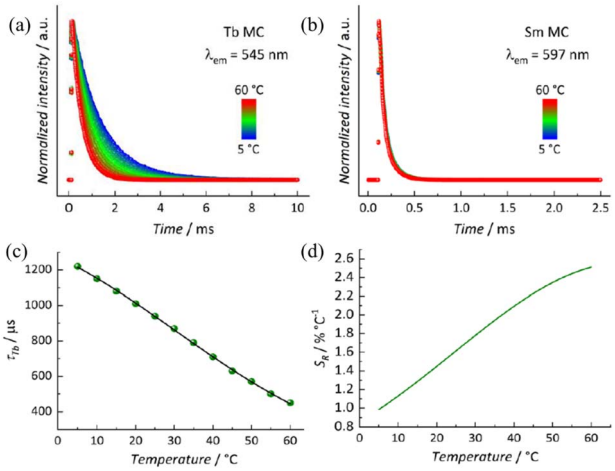

Fig. 5 Varying-temperature emission decay curves of (a) **TbMC** and (b) **SmMC** at $\lambda_{exc} = 336$ nm. (c) Temperature dependence of τ_{Tb} and its fitting with a Boltzmann-like function. Best-fitting parameters: $A_1 = 1.63$, $A_2 = 0.07$, $x_0 = 30.80$, and $r^2 = 0.999$. (d) Relative thermal sensitivity of the thermometric parameter.

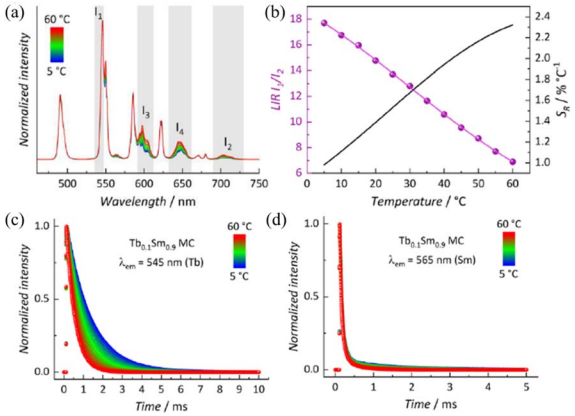

Fig. 6 (a) Varying-temperature emission spectra of $Tb_{0.1}Sm_{0.9}$**MC** at $\lambda_{exc} = 336$ nm. The areas selected for LIR are highlighted in gray. (b) Temperature dependence of LIR (violet) and its fitting with a Boltzmann-like function (best-fitting parameters: $A_1 = 24.35$, $A_2 = 1.05$, $x_0 = 30.10$, and $r^2 = 0.999$) and the relative thermal sensitivity of LIR (black). Varying-temperature emission decay curves of $Tb_{0.1}Sm_{0.9}$**MC** monitoring the (c) Tb $^5D_4$ emission state at 545 nm and (d) Sm $^4G_{5/2}$ emission state at 565 nm.

The relative thermal sensitivity was obtained by applying the fitted function to eqn (2). A maximum relative thermal sensitivity (S_{Rmax}) of 2.51% °C^{-1} was obtained at 60 °C (Fig. 5d). Additionally, the MC has an operational range (S_R > 1% °C^{-1}) within the entire temperature range explored.

$$S_R\ (\%) = [(\partial\Delta/\partial T)/\Delta] \times 100 \quad (2)$$

Due to the significant differences in luminescence intensity and lifetime between Tb^{3+} in **TbMC** and Sm^{3+} in **SmMC**, we developed a novel luminescent mixed-lanthanide thermometer, $Tb_{0.1}Sm_{0.9}$**MC**, which also exhibits high temperature sensitivity. Upon excitation at 336 nm and 20 °C, emission bands corresponding to both Tb^{3+} and Sm^{3+} 4f–4f transitions are observed (Fig. S8†). The bands centered around 600 nm and 650 nm contain emission components from both ions. Although Sm^{3+} is the major constituent of this sample, its emission bands are much less intense than those of Tb^{3+}. This is due to a more efficient sensitization of the Tb^{3+} $^5D_4$ excited state compared to Sm^{3+} $^4G_{5/2}$. Furthermore, Sm^{3+} emission is more susceptible to non-radiative deactivation in solution than Tb^{3+}. Varying-temperature emission spectra were collected from 5 to 60 °C, showing an overall decrease in emission intensity as the temperature is increased (Fig. 6a). The spectra were normalized based on the most intense emission band (545 nm). It was observed that, with increasing temperature, Tb^{3+} emission was quenched more significantly compared to the Sm^{3+} emission, which supports the BET $Tb^{3+} \rightarrow T_1$ process. This also suggests a possible $Tb^{3+} \rightarrow Sm^{3+}$ energy transfer (ET). To perform thermometry measurements using the luminescence intensity ratio (LIR) as the thermometric parameter, two spectral regions were selected: 535–547 nm (I_1) and 689–729 nm (I_2). A Boltzmann-like function was used to fit the temperature dependence of LIR, from which the S_R was derived (Fig. 6b). A S_{Rmax} of 2.33% °C^{-1} was achieved at 60 °C. Two additional ranges, 591–613 nm (I_3) and 631–662 nm (I_4), were also tested, but both yielded a lower overall S_R (Fig. S8†).

To gain further insight into the luminescence dynamics of this system, decay curves were collected by monitoring the emitting states of Tb^{3+} (545 nm) and Sm^{3+} (565 nm). A mono-exponential decay was observed for Tb^{3+} $^5D_4$ (Fig. 6c), while Sm^{3+} $^4G_{5/2}$ exhibited a bi-exponential decay behaviour (Fig. 6d). The lifetime values for both emitting states are summarized in Table S5.† The average lifetime ($\langle\tau\rangle$) of Sm^{3+} was calculated using eqn (3) and applied to the normalized decay curves, where t_0 is the time at which the curves reach their maximum intensity (I) and t_1 is the time at which they reach the background. It is noteworthy that in the $Tb_{0.1}Sm_{0.9}$**MC** system, τ_{Tb} remains similar to the values obtained for **TbMC**, while $\langle\tau_{Sm}\rangle$ is approximately twice as long as that found for **SmMC**. This observation supports the $Tb^{3+} \rightarrow Sm^{3+}$ ET process in the $Tb_{0.1}Sm_{0.9}$**MC** system.

$$\langle\tau\rangle = \frac{\int_{t_0}^{t_1} tI(t)\mathrm{d}t}{\int_{t_0}^{t_1} I(t)\mathrm{d}t} \quad (3)$$

Since τ_{Tb} values were too similar to those obtained for **TbMC**, thermometric calculations were performed using $\langle\tau_{Sm}\rangle$ as the thermometric parameter, yielding a S_{Rmax} of 1.02% °C^{-1} at 49 °C (Fig. S8†). These results suggest that **TbMC** and $Tb_{0.1}Sm_{0.9}$**MC** can function as luminescent thermometers with higher sensitivity than most reported values.[56,57]

Luminescent sensors for Fe^{3+} and DPA

Upon excitation at the ligand-centered absorption band, **TbMC** in ethanol exhibited the characteristic green emission of the Tb^{3+} ion. Given its strong luminescence and long lifetime (Table S4†), we explored its potential as a luminescent sensor. A 1 mg mL^{-1} solution of **TbMC** in ethanol was prepared and uniformly

dispersed using pulsed ultrasound agitation. Various metal ion solutions (K^+, Ca^{2+}, Na^+, Mg^{2+}, Cu^{2+}, Co^{2+}, Ni^{2+}, Mn^{2+}, Cr^{3+}, Ag^+ and Fe^{3+}) of the same concentration were then added to the ethanol solution, and the luminescence intensity was measured before and after the addition to investigate **TbMC**'s response to different metal ions (Fig. 7a). The experimental results indicate that the Fe^{3+} ion caused a rapid decrease in the emission intensity at 545 nm, with a quenching efficiency of 96%, while other metal ions exhibited much milder quenching effects (Fig. 7a). Even in the presence of equal amounts of competing metal ions, Fe^{3+} maintained a high quenching efficiency for the luminescence of **TbMC**, demonstrating its excellent anti-interference ability in selectively detecting Fe^{3+} (Fig. 7b). This further confirms that **TbMC** can serve as a luminescent sensor for the selective detection of Fe^{3+} in organic solvents.

Luminescence titration experiments were conducted to further evaluate the sensitivity of **TbMC** for Fe^{3+} detection (Fig. 7c). As the Fe^{3+} ion concentration increased, the luminescence intensity gradually decreased. Data analysis based on the emission peak at 545 nm revealed that the plot of $I_0/I - 1$ against $[Fe^{3+}]$ exhibited good linear correlation within the low concentration range, which can be described by the Stern–Volmer equation $I_0/I = K_{SV} \times [Fe^{3+}] + 1$ (Fig. 7d). The quenching constant K_{SV} was used to analyze the quenching ability of the Fe^{3+} ion.[58] The LOD at a low Fe^{3+} concentration was determined using the formula LOD $= 3\sigma/K_{SV}$ (where σ represents the standard deviation of the blank measurement).[58] This resulted in an LOD value of 0.51 μM, which is lower than or comparable to the LOD values reported for Ln-based luminescent sensors in the literature.[58–60]

In order to elucidate the luminescence quenching mechanism potentially induced by Fe^{3+}, PXRD and IR spectra were collected before and after detection. The spectra after the sensing experiment were similar to those before being treated with the Fe^{3+} ion, indicating that the **TbMC** structure remained intact and no additional new bonds were generated, which suggest that the luminescence quenching was caused by neither structure collapse nor interacting with the Fe^{3+} ion (Fig. 7e and S1†).[20] Furthermore, the UV-vis absorption spectra of all metal ions are shown in Fig. 7f; the emission spectrum of **TbMC** did not overlap with the UV absorption spectrum of Fe^{3+}, so the possibility of quenching the luminescence by the Förster resonance energy transfer (FRET) mechanism is not considered.[61] While the UV-vis absorption spectrum of the Fe^{3+} ion displayed a strong absorption band between 270 and 350 nm, which significantly overlapped with the excitation spectrum of **TbMC** (Fig. 7f), implying the existence of competition in the absorption of excitation energy between the Fe^{3+} ion and Tb^{3+} ion.[20] Therefore, the addition of the Fe^{3+} ion led to the luminescence quenching of **TbMC**, which is reasonably attributed to the inner filter effect.[62]

DPA, a biomarker for *Bacillus anthracis* spores, plays a crucial in the prevention and control of disease outbreaks.[63] Leveraging the excellent luminescence properties of **TbMC**, we adopted a similar metal ion sensing strategy to investigate its luminescent sensing behaviour towards DPA. Various carboxylic acid solutions of the same concentration were added to the ethanol solution, and only DPA demonstrated effective quenching (Fig. 8a). Additionally, seven potential interferents – benzoic acid (BA), isophthalic acid (IPA), trimesic acid (TA), pyromellitic acid (PMA), nicotinic acid (NA), phenylalanine (Phe), and glycine (Gly) – were tested to evaluate the anti-interference performance of **TbMC** (Fig. 8b). The results indicate that these interferents did not affect the detection of DPA by **TbMC**, confirming its high selectivity as a luminescent sensor for DPA. As shown in Fig. 8c, increasing the DPA concentration significantly decreased the intensity of all the bands, which was observed as a noticeable decrease in green emission. At low concentrations, the Stern–Volmer plot for DPA shows a strong linear correlation between the luminescence intensity and DPA concentration (R^2 = 0.9860) (Fig. 8d), yielding a quenching

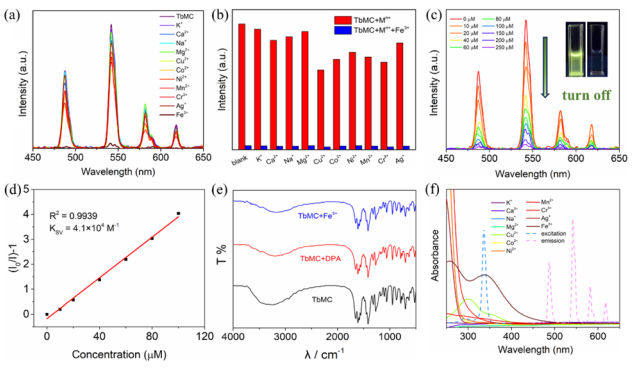

Fig. 7 (a) Luminescence emission spectra of **TbMC** in ethanol before and after addition of different metal ions. (b) Relative luminescence intensity of **TbMC** at 545 nm for Fe^{3+} sensing without and with competing metal ions. (c) Luminescence emission spectra of **TbMC** with gradually increasing Fe^{3+} concentration. (d) Linear plot of $I_0/I - 1$ against Fe^{3+} concentrations. (e) IR spectra of **TbMC** before and after treatment with Fe^{3+} and DPA in ethanol at room temperature for 12 h. (f) UV-vis absorption spectra of metal ions and the excitation and emission spectra of **TbMC** in ethanol.

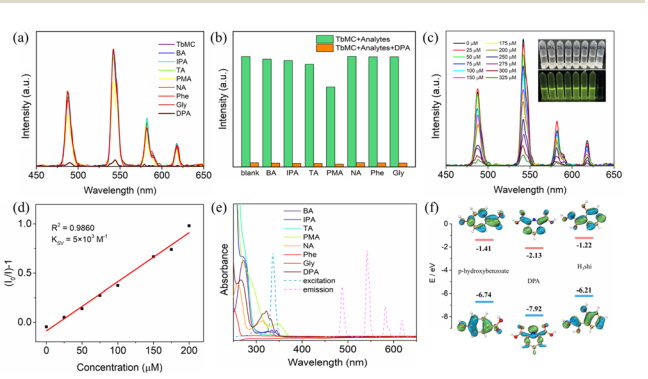

Fig. 8 (a) Luminescence emission spectra of **TbMC** in ethanol before and after addition of various carboxylic acids. (b) Relative luminescence intensity of **TbMC** at 545 nm for DPA sensing without and with various carboxylic acids. (c) Luminescence emission spectra of **TbMC** with gradually increasing DPA concentration. (d) Linear plot of $I_0/I - 1$ against DPA concentrations. (e) UV-vis absorption spectra of various carboxylic acids and the excitation and emission spectra of **TbMC** in ethanol. (f) HOMO and LUMO energy levels for ligands and DPA.

constant K_{SV} of 5×10^3 M^{-1}. The LOD was calculated to be 4.26 μM, which is significantly lower than the infectious dose of anthrax spores (60 mM).[64] These results suggest that **TbMC** is an ideal candidate for the luminescent detection of anthrax spores.

To investigate the potential DPA sensing mechanism of **TbMC**, we analyzed the PXRD (Fig. S3†) and IR (Fig. 7e) results. It is evident that the luminescence quenching of **TbMC** is neither due to the collapse of the framework nor due to the formation of new coordination or hydrogen bonds with DPA molecules. The UV-vis absorption spectrum of DPA significantly overlaps with the excitation spectrum of **TbMC** but not with its emission spectrum (Fig. 8e). This overlap indicates that the luminescence quenching is caused by the inner filter effect due to competitive absorption of the excitation spectrum energy, rather than by the FRET mechanism.[65] Additionally, the calculated LUMO energy levels of ligands sodium *p*-hydroxybenzoate and H_3shi are −1.41 and −1.22 eV, respectively, whereas DPA has a much lower LUMO energy level of −2.13 eV (Fig. 8f). This calculation suggests that the quenching of lanthanide luminescence is likely due to photoinduced electron transfer, with electrons moving from the LUMO of the ligands to the LUMO of DPA, thereby causing luminescence quenching.[37] In summary, the experimental results indicate that DPA induces luminescence quenching in **TbMC** through multiple mechanisms.

At the same time, the luminescent sensor test papers for detecting Fe^{3+} and DPA were prepared to further evaluate the practical applications of **TbMC**. As shown in Fig. 9, blank test papers were immersed in a 1 mg mL^{-1} **TbMC** solution and subsequently dried under vacuum. Only the sections exposed to Fe^{3+} and DPA showed the disappearance of green luminescence under UV light, while no colour change was observed for other substances. The successful preparation of these test papers highlights the potential of **TbMC** as a luminescent sensor for detecting Fe^{3+} and the anthrax biomarker DPA, indicating promising applications in public health and safety.

LnMC's anti-counterfeiting inks and films

The use of anti-counterfeiting inks to verify product authenticity and protect documents is critical to global commerce, information security and public health.[66] **LnMC** is an ideal candidate for the development of anti-counterfeiting inks due to its excellent luminescence properties and multicolour tunability in the visible region. Therefore, we selected **SmMC**, **$Tb_{0.1}Sm_{0.9}$MC** and **TbMC** with bright emission colours to be dispersed in DMF to make multicolour luminescent inks that can be used to draw patterns or encrypt information (Fig. 10a). A beautiful flower pattern was created in which the petals were drawn in **SmMC** ink, the stamens in **$Tb_{0.1}Sm_{0.9}$MC** ink and the leaves in **TbMC** ink. Such pattern is invisible in daylight but visible under UV light where the vibrant colours were clearly recognizable and can be used to identify authenticity (Fig. 10b). Furthermore, a strategy was devised to encrypt the information using disrupted letters; "YES NO" was encrypted as "YNEOS", where "YES" was written in **TbMC** ink and "NO" in **SmMC** ink, and they can be recognized only when properly aligned under UV light (Fig. 10c). To increase the level of encryption for information security, triple encryption was implemented using ASCII binary codes (Fig. 10d). The code created using **SmMC** and **TbMC** is not visible in daylight. The decryption consists of three steps: first, the luminous dots are recognized under UV light; second, the green and red luminous dots are converted to binary codes "0" and "1", respectively; and third, the corresponding letters are decrypted according to the ASCII binary code "NICE" (Fig. 10d). The luminescence responsiveness of Fe^{3+} and DPA has led to the emergence of erasable luminescent inks, where we can selectively leave or erase luminescent information to regulate its visibility or invisibility on demand. As shown in Fig. 10e, a colourful pattern was drawn using the three inks, some of the luminescence was quenched with two erasing agents (an ethanolic solution of 300 μM Fe^{3+} or DPA), and the retained luminescence pattern eventually showed the information "HLJU" (the acronym of Heilongjiang University) under UV light. These results demonstrate that the luminescent inks are simple, convenient, and efficient anti-counterfeiting materials and can greatly improve the security of information by cleverly designing various encryption strategies.

Luminescent films have attracted a lot of attention due to their unique properties with potential applications in optical devices, sensors and anti-counterfeiting labels.[67] In view of the

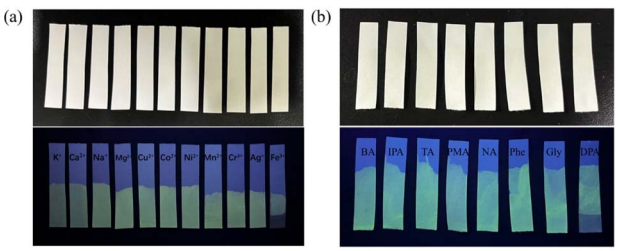

Fig. 9 (a) Luminescence photographs of **TbMC** under daylight and under UV light with metal ions. (b) Luminescence photographs of **TbMC** under daylight and under UV light with carboxylic acids.

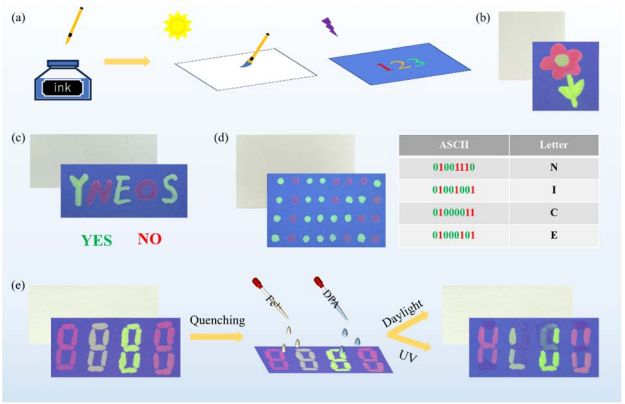

Fig. 10 (a) Schematic of writing information with luminescent inks. (b) Digital images of a flower painted by using **SmMC**, **$Tb_{0.1}Sm_{0.9}$MC** and **TbMC**. (c) The double encryption of the phrase "YES NO". (d) "NICE" encrypted by the ASCII binary code. (e) Encryption and decryption process of patterns based on Fe^{3+} and DPA luminescence quenching effects.

stability of **LnMC** in solvents and multicolour luminescence properties, **PMMA/LnMC** (Ln = Sm, $Tb_{0.1}Sm_{0.9}$ and Tb) luminescent films were successfully prepared by doping **LnMC** into a polymethylmethacrylate (PMMA) matrix (Fig. 11a). These films exhibit bright red, yellow, and green luminescence under UV light, respectively, and show high transparency over 90% (Fig. S9†) allowing clear patterns to be observed through the films under both daylight and UV light (Fig. 11b). In addition, the flexibility of the films enables them to be easily fabricated into special shapes or cut to any size to meet a variety of needs (Fig. 11c). Accordingly, the **LnMC** films were cut and assembled into a variety of patterns for further development into anti-counterfeiting labels, which can be directly attached to glass bottles, washing bottles and rulers (Fig. 11d–f). Exposing the labels to UV light showed rich colours, whereas only the transparent films could be observed under natural light (Fig. 11d–f), effectively improving the level of anti-counterfeiting. More interestingly, we developed a new type of anti-counterfeiting barcode by utilizing the quenching effect of Fe^{3+} and DPA on **TbMC** luminescence. Under daylight, no information can be recognized by scanning the barcode through the film, but only under UV light the quenched parts of Fe^{3+} and DPA can be identified as black lines used to assemble a new barcode, which can be recognized by a mobile phone to get the correct information "HLJU" that was hidden (Fig. 11g). Obviously, **LnMC** films reveal high transparency, good luminescence properties and extraordinary processability, thereby becoming a candidate material for the anti-counterfeiting and information encryption.

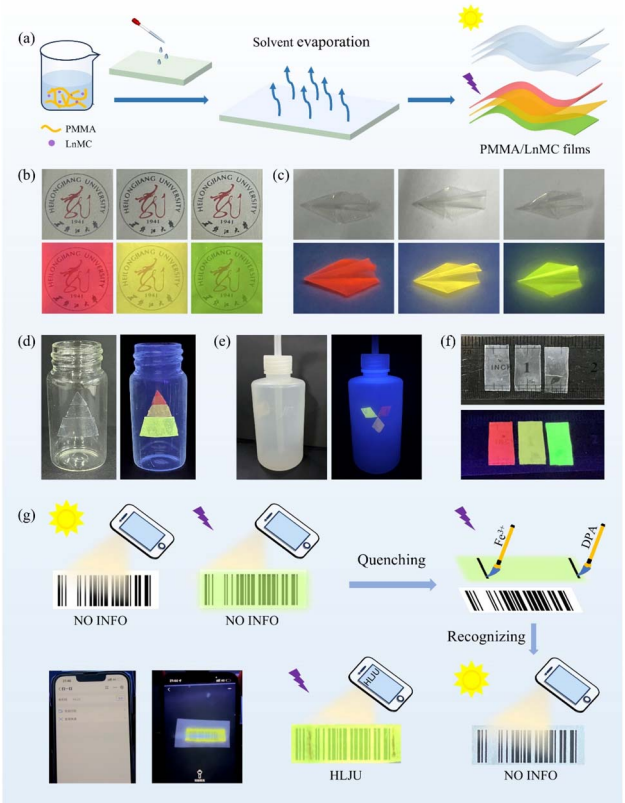

Fig. 11 (a) Schematic diagram of the preparation process of PMMA/LnMC films. (b) The digital photos of PMMA/LnMC films under daylight and UV light. (c) The digital photos of "airplane" shaped PMMA/LnMC films under daylight and UV light. (d–f) The digital photos of PMMA/LnMC films used as luminescent anti-counterfeiting labels: glass bottles, wash bottles and rulers. (g) Encryption and decryption process of barcode based on Fe^{3+} and DPA luminescence quenching effects.

Conclusions

In conclusion, a series of novel Ln^{3+}/Al^{3+} MCs were successfully constructed with multifunctional applications. **LnMC** exhibited photoluminescence in almost the full spectral range from visible to near-infrared, and luminescence modulation was accomplished by adjusting the molar ratio of Tb^{3+} and Sm^{3+} ions. Based on the excellent luminescence performance of **LnMC**, it has been successfully developed for the detection of LFPs, which can be clearly identified even with the third level of details, and has potential application value in criminal investigation. In addition, **TbMC** and $\mathbf{Tb_{0.1}Sm_{0.9}MC}$ possess potential as luminescent thermometers, with high sensitivities of 2.51% $°C^{-1}$ and 2.33% $°C^{-1}$, respectively, in the temperature range of 5–60 °C. Meanwhile, **TbMC** represents the first multi-responsive MC luminescent sensor that could rapidly and selectively detect Fe^{3+} and DPA, and the success of the test paper proved its practical applicability. More strikingly, **LnMC** can also be functionalized into luminescent inks and films to effectively improve the level of anti-counterfeiting. On the whole, the Ln^{3+}/Al^{3+} MCs present excellent luminescence properties, making them promising multifunctional luminescent sensors and anti-counterfeiting materials.

Data availability

The data supporting this article have been included as part of the ESI.† Crystallographic data for DyMC have been deposited at the CCDC (2377154).

Author contributions

Han Yan: conceptualization, investigation, data curation, writing – original draft. Claudia M. S. Calado: data curation and writing – original draft. Hao Wang: formal analysis. Muralee Murugesu: supervision and methodology. Wen-Bin Sun: supervision, methodology, writing – reviewing and editing.

Conflicts of interest

There are no conflicts to declare.

Acknowledgements

This work was supported by National Natural Science Foundation of China (22071047) and Natural Science Foundation of Heilongjiang Province (PL2024B013). All experiments were performed in compliance with relevant laws or guidelines; the

volunteer was informed and consented to the use of their fingerprints.

Notes and references

1 M. Tegoni and M. Remelli, *Coord. Chem. Rev.*, 2012, **256**, 289–315.
2 G. Mezei, C. M. Zaleski and V. L. Pecoraro, *Chem. Rev.*, 2007, **107**, 4933–5003.
3 M. S. Lah and V. L. Pecoraro, *J. Am. Chem. Soc.*, 1989, **111**, 7258–7259.
4 S. H. Seda, J. Janczak and J. Lisowski, *Inorg. Chem. Commun.*, 2006, **9**, 792–796.
5 J. Jankolovits, J. W. Kampf and V. L. Pecoraro, *Polyhedron*, 2013, **52**, 491–499.
6 C.-S. Lim, J. Jankolovits, P. Zhao, J. W. Kampf and V. L. Pecoraro, *Inorg. Chem.*, 2011, **50**, 4832–4841.
7 C.-S. Lim, J. W. Kampf and V. L. Pecoraro, *Inorg. Chem.*, 2009, **48**, 5224–5233.
8 A. Maspero, S. Brenna, S. Galli and A. Penoni, *J. Organomet. Chem.*, 2003, **672**, 123–129.
9 M. Casarin, C. Corvaja, C. di Nicola, D. Falcomer, L. Franco, M. Monari, L. Pandolfo, C. Pettinari, F. Piccinelli and P. Tagliatesta, *Inorg. Chem.*, 2004, **43**, 5865–5876.
10 C. Dendrinou-Samara, A. N. Papadopoulos, D. A. Malamatari, A. Tarushi, C. P. Raptopoulou, A. Terzis, E. Samaras and D. P. Kessissoglou, *J. Inorg. Biochem.*, 2005, **99**, 864–875.
11 M. Alexiou, I. Tsivikas, C. Dendrinou-Samara, A. A. Pantazaki, P. Trikalitis, N. Lalioti, D. A. Kyriakidis and D. P. Kessissoglou, *J. Inorg. Biochem.*, 2003, **93**, 256–264.
12 S.-G. Wu, Z.-Y. Ruan, G.-Z. Huang, J.-Y. Zheng, V. Vieru, G. Taran, J. Wang, Y.-C. Chen, J.-L. Liu, L. T. A. Ho, L. F. Chibotaru, W. Wernsdorfer, X.-M. Chen and M.-L. Tong, *Chem*, 2021, **7**, 982–992.
13 X. Wen, H. Li, Z. Ju, R. Deng and D. Parker, *Chem. Sci.*, 2024, **15**, 19944–19951.
14 J. Wang, Q.-W. Li, S.-G. Wu, Y.-C. Chen, R.-C. Wan, G.-Z. Huang, Y. Liu, J.-L. Liu, D. Reta, M. J. Giansiracusa, Z.-X. Wang, N. F. Chilton and M.-L. Tong, *Angew. Chem., Int. Ed.*, 2021, **60**, 5299–5306.
15 Y. Cui, B. Chen and G. Qian, *Coord. Chem. Rev.*, 2014, **273–274**, 76–86.
16 Y. Zou, W. Lv, Z. Xue, J. Pan, X.-Y. Li and G.-M. Wang, *Dalton Trans.*, 2022, **51**, 16383–16388.
17 Y.-J. Ma, F. Xu, X.-Y. Ren, F.-Y. Chen, J. Pan, J.-H. Li, S.-D. Han and G.-M. Wang, *Chem. Sci.*, 2024, **15**, 17642–17651.
18 S. E. Bodman and S. J. Butler, *Chem. Sci.*, 2021, **12**, 2716–2734.
19 J.-C. G. Bünzli and C. Piguet, *Chem. Soc. Rev.*, 2005, **34**, 1048–1077.
20 Z.-J. Hu, M.-J. Tsai, Y.-J. Tu and J.-Y. Wu, *Chem.–Eur. J.*, 2023, **29**, e202300081.
21 J. Jankolovits, C. M. Andolina, J. W. Kampf, K. N. Raymond and V. L. Pecoraro, *Angew. Chem., Int. Ed.*, 2011, **50**, 9660–9664.
22 S. V. Eliseeva, E. V. Salerno, B. A. Lopez Bermudez, S. Petoud and V. L. Pecoraro, *J. Am. Chem. Soc.*, 2020, **142**, 16173–16176.
23 T. N. Nguyen, C. Y. Chow, S. V. Eliseeva, E. R. Trivedi, J. W. Kampf, I. Martinić, S. Petoud and V. L. Pecoraro, *Chem.–Eur. J.*, 2018, **24**, 1031–1035.
24 T. N. Nguyen, S. V. Eliseeva, C. Y. Chow, J. W. Kampf, S. Petoud and V. L. Pecoraro, *Inorg. Chem. Front.*, 2020, **7**, 1553–1563.
25 E. V. Salerno, S. V. Eliseeva, B. L. Schneider, J. W. Kampf, S. Petoud and V. L. Pecoraro, *J. Phys. Chem. A*, 2020, **124**, 10550–10564.
26 E. V. Salerno, A. N. Carneiro Neto, S. V. Eliseeva, M. A. Hernández-Rodríguez, J. C. Lutter, T. Lathion, J. W. Kampf, S. Petoud, L. D. Carlos and V. L. Pecoraro, *J. Am. Chem. Soc.*, 2022, **144**, 18259–18271.
27 M. Y. Zhuang, H. Yang, H. G. Zhang, H. Q. Tian, D. C. Li and J. M. Dou, *Transition Met. Chem.*, 2022, **47**, 139–146.
28 J. Cao, R. Chen, L. Wang, H. Xing, H. Hu, X. Yang, C. Gu, S. Tang and D. Chen, *Chem. Eng. J.*, 2024, **491**, 152121.
29 L. Li, P. Xi, Q. Li, X. Wang and B. Cheng, *Colloids Surf., A*, 2022, **652**, 129759.
30 X. Zhao, Z. Liu, Y. Duan, Z. Xu, X. Feng, Z. Li and T. Han, *Chem. Eng. J.*, 2024, **498**, 155525.
31 X. Lin, M. Kong, N. Wu, Y. Gu, X. Qiu, X. Chen, Z. Li, W. Feng and F. Li, *ACS Appl. Mater. Interfaces*, 2020, **12**, 52393–52401.
32 S.-N. Zhao, L.-J. Li, X.-Z. Song, M. Zhu, Z.-M. Hao, X. Meng, L.-L. Wu, J. Feng, S.-Y. Song, C. Wang and H.-J. Zhang, *Adv. Funct. Mater.*, 2015, **25**, 1463–1469.
33 J.-J. Pang, Z.-Q. Yao, K. Zhang, Q.-W. Li, Z.-X. Fu, R. Zheng, W. Li, J. Xu and X.-H. Bu, *Angew. Chem., Int. Ed.*, 2023, **62**, e202217456.
34 H. Guan, M. Qi, L. Shi, W. Liu, L. Yang and W. Dou, *ACS Appl. Mater. Interfaces*, 2023, **15**, 18114–18124.
35 D. Errulat, R. Marin, D. A. Gálico, K. L. M. Harriman, A. Pialat, B. Gabidullin, F. Iikawa, O. D. D. Couto Jr, J. O. Moilanen, E. Hemmer, F. A. Sigoli and M. Murugesu, *ACS Cent. Sci.*, 2019, **5**, 1187–1198.
36 D. Ananias, F. A. A. Paz, D. S. Yufit, L. D. Carlos and J. Rocha, *J. Am. Chem. Soc.*, 2015, **137**, 3051–3058.
37 Y. Cui, H. Xu, Y. Yue, Z. Guo, J. Yu, Z. Chen, J. Gao, Y. Yang, G. Qian and B. Chen, *J. Am. Chem. Soc.*, 2012, **134**, 3979–3982.
38 X. Wang, K. Gopalsamy, G. Clavier, G. Maurin, B. Ding, A. Tissot and C. Serre, *Chem. Sci.*, 2024, **15**, 6488–6499.
39 X. Wang, G. Clavier, Y. Zhang, K. Batra, N. Xiao, G. Maurin, B. Ding, A. Tissot and C. Serre, *Chem. Sci.*, 2023, **14**, 5386–5395.
40 D.-M. Chen, N.-N. Zhang, C.-S. Liu and M. Du, *J. Mater. Chem. C*, 2017, **5**, 2311–2317.
41 X. Leng, W. Hao, X. Yang, Z. Zhang, H. Li, Y. Ma, Y. Cheng and D. Schipper, *Inorg. Chem.*, 2022, **61**, 8484–8489.
42 S. Yang, J. Lin, S. Wang, X. Wu, D. Schipper and X. Yang, *Anal. Chem.*, 2024, **96**, 19093–19099.
43 J.-Q. Zhao, H.-S. Shi, L.-R. Zeng, H. Ge, Y.-H. Hou, X.-M. Wu, C.-Y. Yue and X.-W. Lei, *Chem. Eng. J.*, 2022, **431**, 134336.

44 X. Yu, A. A. Ryadun, D. I. Pavlov, T. Y. Guselnikova, A. S. Potapov and V. P. Fedin, *Angew. Chem., Int. Ed.*, 2023, **62**, e202306680.
45 C. Zhuo, S. Zhao, X. Huang, Y. Jiang, J. Li and D.-Y. Fu, *J. Mol. Liq.*, 2023, **376**, 121442.
46 Q. Luo, J. Jiang, S. Yang, D. Li, J. Dai, X. Wang, Y. Xu, B. Zeng, W. Luo, C. Yuan and L. Dai, *Chem. Eng. J.*, 2024, **490**, 151898.
47 S. Alvarez, P. Alemany, D. Casanova, J. Cirera, M. Llunell and D. Avnir, *Coord. Chem. Rev.*, 2005, **249**, 1693–1708.
48 X. Wang, H. Chang, J. Xie, B. Zhao, B. Liu, S. Xu, W. Pei, N. Ren, L. Huang and W. Huang, *Coord. Chem. Rev.*, 2014, **273–274**, 201–212.
49 S. V. Eliseeva, T. N. Nguyen, J. W. Kampf, E. R. Trivedi, V. L. Pecoraro and S. Petoud, *Chem. Sci.*, 2022, **13**, 2919–2931.
50 C. Y. Chow, S. V. Eliseeva, E. R. Trivedi, T. N. Nguyen, J. W. Kampf, S. Petoud and V. L. Pecoraro, *J. Am. Chem. Soc.*, 2016, **138**, 5100–5109.
51 S. Yang, C.-F. Wang and S. Chen, *Angew. Chem., Int. Ed.*, 2011, **50**, 3706–3709.
52 G. P. Darshan, H. B. Premkumar, H. Nagabhushana, S. C. Sharma, S. C. Prashanth and B. D. Prasad, *J. Colloid Interface Sci.*, 2016, **464**, 206–218.
53 P. Pan, T. Zhang, B. Yu, R. Ma, Q. Yue, A. A. Alghamdi and Y. Deng, *J. Colloid Interface Sci.*, 2022, **605**, 425–431.
54 Z. Lv, Z. Man, Z. Xu, S. Li, Q. Liao and H. Fu, *J. Mater. Chem. C*, 2021, **9**, 7345–7350.
55 L. Li, Q. Li, J. Chu, P. Xi, C. Wang, R. Liu, X. Wang and B. Cheng, *Appl. Surf. Sci.*, 2022, **581**, 152395.
56 X. Chen, S. Liu, K. Huang, J. Nie, R. Kang, X. Tian, S. Zhang, Y. Li and J. Qiu, *Chem. Eng. J.*, 2020, **396**, 125201.
57 K. Elzbieciak-Piecka, M. Suta and L. Marciniak, *Chem. Eng. J.*, 2021, **421**, 129757.
58 X. Wang, S. He, J. Chen, J. Wei, C. Chen, W. Shi, D. Wu, L. Fu and T. Yang, *Dalton Trans.*, 2024, **53**, 276–284.
59 B. B. Rath and J. J. Vittal, *Inorg. Chem.*, 2020, **59**, 8818–8826.
60 S. Y. Hao, S. X. Hou, Z. C. Hao and G. H. Cui, *Spectrochim. Acta, Part A*, 2018, **189**, 613–620.
61 L. Wu, C. Huang, B. P. Emery, A. C. Sedgwick, S. D. Bull, X.-P. He, H. Tian, J. Yoon, J. L. Sessler and T. D. James, *Chem. Soc. Rev.*, 2020, **49**, 5110–5139.
62 J.-Q. Wu, X.-Y. Ma, C.-L. Liang, J.-M. Lu, Q. Shi and L.-X. Shao, *Dalton Trans.*, 2022, **51**, 2890–2897.
63 D. D. Evanoff, J. Heckel, T. P. Caldwell, K. A. Christensen and G. Chumanov, *J. Am. Chem. Soc.*, 2006, **128**, 12618–12619.
64 M. D. Yilmaz and H. A. Oktem, *Anal. Chem.*, 2018, **90**, 4221–4225.
65 Y. Ma, X. Yang, Z. Xiao, X. Liu, D. Shi, M. Niu and D. Schipper, *Chem. Commun.*, 2021, **57**, 7316–7319.
66 H. Zhou, J. Han, J. Cuan and Y. Zhou, *Chem. Eng. J.*, 2022, **431**, 134170.
67 R. Gao, X. Fang and D. Yan, *J. Mater. Chem. C*, 2019, **7**, 3399–3412.